OPEN ACCESS

Catalysis & Surface ARTICLE

The Innovation Energy

Cascade catalysts from heavy bio-oil for plasma-catalytic NH_3 synthesis

Feng Gong,[1,*] Juntao Bao,[1] Yuhang Jing,[1] Qiang Zhou,[2] Chaozhen Liu,[3] Shaohuan Hong,[1] Zhiqi Zhang,[1] Weiwei Fan,[1] Hualin Ye,[4] and Rui Xiao[1,*]

*Correspondence: gongfeng@seu.edu.cn (G.F.); ruixiao@seu.edu.cn (X.R.)

Received: March 27, 2026; Accepted: May 14, 2026; Published Online: July 18, 2026; https://doi.org/10.59717/j.xinn-energy.2026.100178

GRAPHICAL ABSTRACT

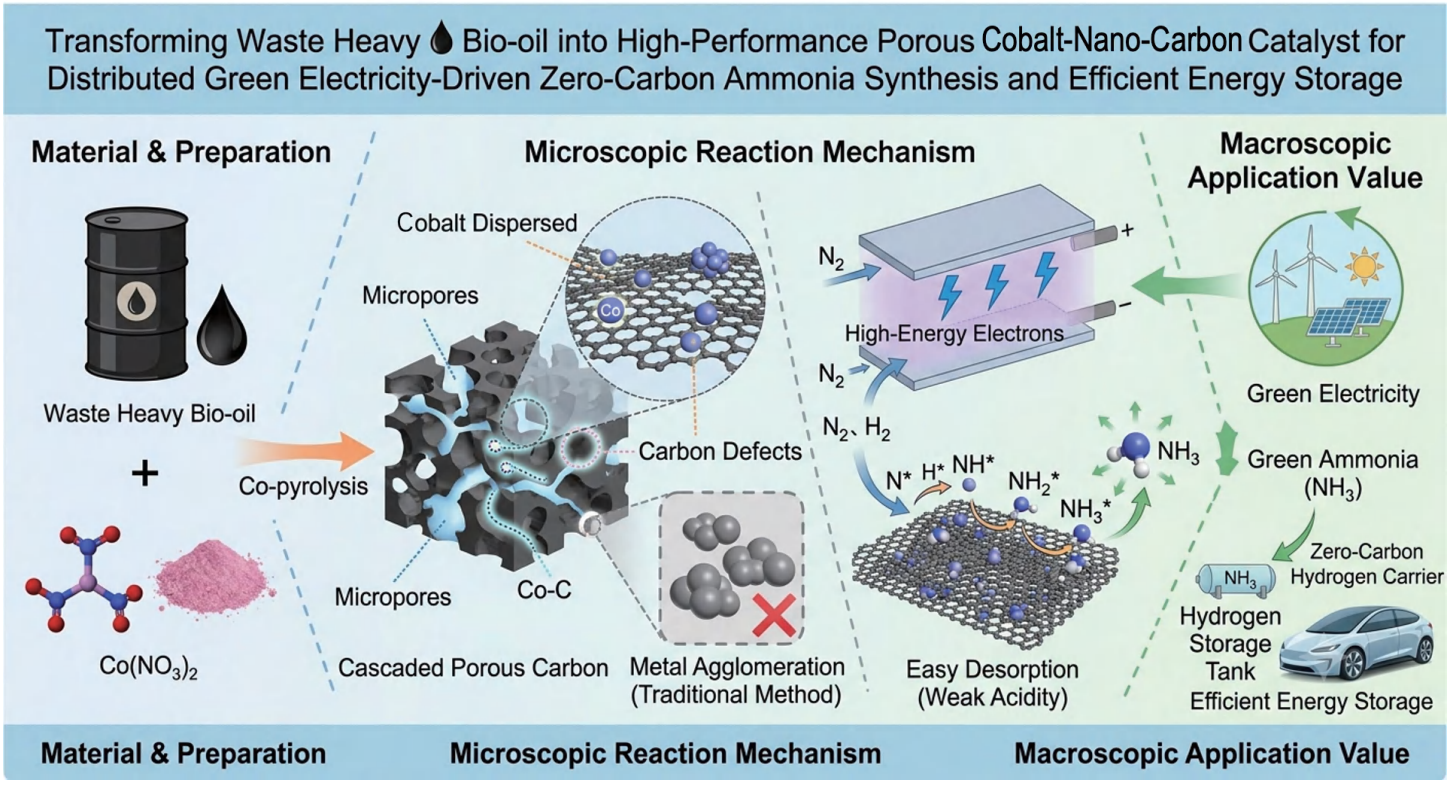

PUBLIC SUMMARY

- Plasma-assisted ammonia synthesis (PAAS) operates under ambient conditions and supports distributed renewable energy storage, yet traditional PAAS catalysts suffer low efficiency and high costs.
- Novel cascade porous Co-doped biochar catalysts (Co-PB) are fabricated from waste heavy bio-oil with uniform cobalt dispersion and abundant carbon-cobalt bonding.
- Co-PB accelerates interfacial electron and radical transfer, reaching an ammonia synthesis rate of 1.605 mmol/g·h with outstanding cycling stability.
- Economic and environmental evaluations verify the great application prospect of this waste-derived catalyst for sustainable green energy storage.

ARTICLE Catalysis & Surface

www.the-innovation.org/the-innovation-energy

Cascade catalysts from heavy bio-oil for plasma-catalytic NH_3 synthesis

Feng Gong,[1,*] Juntao Bao,[1] Yuhang Jing,[1] Qiang Zhou,[2] Chaozhen Liu,[3] Shaohuan Hong,[1] Zhiqi Zhang,[1] Weiwei Fan,[1] Hualin Ye,[4] and Rui Xiao[1,*]

[1]School of Energy and Environment, Southeast University, Nanjing 211100, China

[2]School of Engineering, The University of Tokyo, Tokyo 113-8656, Japan

[3]State Key Laboratory of Clean Energy Utilization, Zhejiang University, Hangzhou 310027, China

[4]Jiangsu Key Laboratory of New Power Batteries, Jiangsu Collaborative Innovation Center of Biomedical Functional Materials, School of Chemistry and Materials Science, Nanjing Normal University, Nanjing 210023, China

*Correspondence: gongfeng@seu.edu.cn (G.F.); ruixiao@seu.edu.cn (X.R.)

Received: March 27, 2026; Accepted: May 14, 2026; Published Online: July 18, 2026; https://doi.org/10.59717/j.xinn-energy.2026.100178

Citation: Gong F., Bao J., Jing Y., et al. (2026). Cascade catalysts from heavy bio-oil for plasma-catalytic NH_3 synthesis. *The Innovation Energy* **3**:100178.

Plasma-assisted ammonia synthesis (PAAS) enables the production of ammonia at ambient temperature and pressure by utilizing high-energy free electrons to break N≡N and H-H bonds. This process leverages green electricity and hydrogen, offering an efficient and distributed alternative for renewable energy storage. However, conventional catalysts used in PAAS (Al_2O_3, metal-organic frameworks, molecular sieves, etc.) suffer from low efficiency, poor cycling performance, and high cost. Herein, we design and develop novel cascade porous biochar-based catalysts (Co-PB) derived from waste heavy bio-oil through catalytic pyrolysis by using cobalt nitrate as a pyrolysis catalyst, giving rise to a highly porous structure with uniformly distributed Co in Co-PB. The good mobility of heavy bio-oil ensures homogeneous C-Co bonds, which further enhances the transfer kinetics of the interfacial electron and the radical. As a result, Co-PB achieves a high PAAS rate of 1.605 mmol/g·h and exhibits excellent stability and cyclability under harsh electric fields. Economic and environmental assessments highlight the significant potential of PAAS for sustainable hydrogen and electricity storage.

INTRODUCTION

Ammonia is a crucial chemical feedstock and one of the most produced inorganic materials globally.[1,2] Owing to its unique advantages of high hydrogen storage density (17.7 wt%), cleanliness, efficiency, and renewability, ammonia is also universally appreciated as zero-carbon fuel and hydrogen carrier.[3-5] However, the conventional ammonia synthesis—Haber-Bosch (H-B) process requires extremely harsh conditions, such as temperatures up to 500 °C and pressures ranging from 200 to 500 bar.[6-9] The centralized H-B process consumes 2% of the world's energy and emits more than 420 million tons of CO_2 annually, posing a significant challenge to achieve the global carbon neutrality.[10,11] As a result, there has been a growing interest in developing emerging green and low-carbon technologies for ammonia synthesis using renewable energy sources. These technologies include photocatalytic ammonia synthesis,[12-14] electrochemical ammonia synthesis,[15-17] chemical looping ammonia synthesis,[18-21] and biological nitrogen fixation.[22-27] While these green and distributed alternatives offer the potential for hydrogen and renewable energy storage through ammonia, the low ammonia synthesis rates severely limit the development of these methods.[28,29]

The plasma-assisted ammonia synthesis (PAAS) can be coupled with distributed renewable electricity to synthesize ammonia using H_2 and N_2 through a zero-carbon process at ambient pressure.[30,31] This process even has a higher theoretical rate of ammonia synthesis than that of the H-B process, providing a green and efficient alternative for ammonia synthesis.[30,31] Unlike the H-B process, PAAS excites molecules into radicals using high-energy electrons to enhance the reaction on catalysts. As a result, PAAS does not require harsh conditions of high temperature and pressure to promote N_2 dissociation. [32,33] PAAS can be accomplished using only electricity for plasma generation, which can effectively integrate with renewable electricity from solar and wind. This enables PAAS to be applied in remote areas, saving the cost and energy consumption for ammonia transportation. [34,35]

Currently, the widely used catalysts in PAAS include Al_2O_3, [36,37] SiO_2, [38,39] mesoporous molecular sieves,[40] and metal-organic frameworks.[41,42] These catalysts possess porous structure and large specific surface area, which increase the number of active sites. However, a drawback is the difficulty in modulating the pore structure to improve the PAAS performance. Moreover, these materials generally have high costs and their structures are prone to collapse and inactivate under prolonged exposure to strong electrics.[34,43]

In recent years, it has been increasingly recognized that the electronic structure of the catalyst surface plays a decisive role in the activation of reactants (especially N_2) and the stabilization of intermediates during the plasma catalysis. By tailoring the electronic properties of the catalyst, the adsorption and conversion efficiency of high energy electrons, excited species, and free radicals can be optimized, thereby enhancing the ammonia synthesis performance.[44] For example, the defect engineering can reconstruct the electronic density of states of active sites, enhance the charge transfer, and thus promote the dissociation of the N≡N bond. More importantly, the plasma itself can induce strong metal support interactions at low temperatures, leading to significant charge redistribution between the metal species and the support; this plasma driven electronic effect has been demonstrated to markedly improve the catalytic activity.[45] In non noble metal systems, strategies such as heteroatom doping or the construction of metal carbon covalent bonds (e.g., Co—C bonds) to modulate the surface acidity and electron donor ability have also been proven effective in increasing the efficiency of plasma catalytic ammonia synthesis.[46,47] Nevertheless, most reported electronic modulation methods still rely on complex multi step synthesis or expensive raw materials, and the synergistic mechanism between the electron transfer pathway and plasma discharge characteristics remains poorly understood. Therefore, the development of a catalyst preparation strategy that combines structural tunability, low cost, and efficient electronic modulation is of great significance for advancing PAAS technology.

Heavy bio-oil (also known as bio-tar), a waste product from biomass pyrolysis, can be utilized as an ashless source to prepare biochar. This offers the advantage of removing the original biomass skeleton and easily regulating the framework structure of the obtained biochar.[48] Meanwhile, the main recycle solution for waste heavy bio-oil is combustion for heat supply, causing serious pollution and energy loss.[49] Therefore, converting heavy bio-oils into valuable biochar is a prospective way to address this challenge. Porous biochar, prepared from heavy bio-oil, is an inexpensive material with easily regulated pore structure and large specific surface area. The interconnected graded pores (micro-, meso-, macro-pores) in biochar can enhance the mass transfer of free radicals, while the high surface area of biochar can increase the number of active sites, making biochar a promising PAAS catalyst. However, as far as we know, biochar-based catalysts made from heavy bio-oil for PAAS have not been reported yet. Therefore, it is of great significance to explore simple and efficient methods to develop high-performance biochar-based catalysts for PAAS from heavy bio-oil.

In this study, we develop a high-performance biochar-based cobalt catalyst (Co-PB) for PAAS by directly preparing it from the co-catalytic pyrolysis of heavy bio-oil—an industrial waste. Cobalt, as a co-catalytic pyrolysis catalyst, promotes the pyrolysis of heavy bio-oil and results in a biochar framework with a more pronounced porous structure. The co-catalytic pyrolysis method also brings about a more uniform distribution of the active cobalt metal, thereby enhancing the PAAS performance. This is a "dual-function strategy" approach for catalyst design. The PAAS performances of catalysts

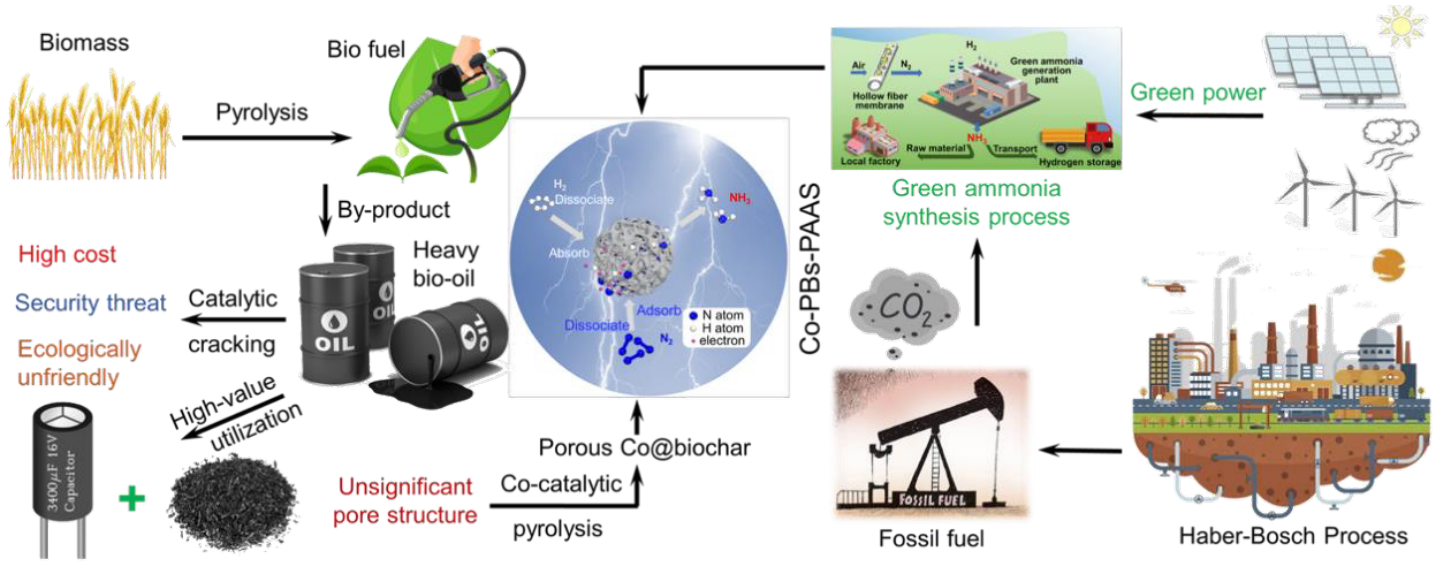

Figure 1. Schematic diagram of the green ammonia industry using the distributed renewable electricity (wind, solar, etc.): valorizing heavy bio-oil, an industrial by-product, for green ammonia synthesis, aiming to break the limits of the centralized Haber-Bosch process.

prepared using different methods demonstrate the superiority of the co-catalytic pyrolysis. The impact of the co-catalytic catalyst on the structural properties, morphology, and PAAS performance of the products is thoroughly investigated. This study successfully elucidates the mechanism behind the enhancement in PAAS performance of Co-PB through systematic characterizations and multi-scale modeling. The analysis of the economic and environmental competitiveness of an ideal PAAS plant demonstrates its high potential for practical applications. The preparation of Co-PB catalysts for PAAS from heavy bio-oil not only avoids the cost and environmental hazards of catalytic cracking treatment, but also provides a proven strategy for future green ammonia synthesis process (Figure 1). The dielectric barrier discharge (DBD) plasma employed for the PAAS experiments is described in detail in the Supporting Information (Figure S1).

MATERIALS AND METHODS

Catalyst preparation

In a typical experiment, 10 g heavy bio-oil (an industrial by-product from the pyrolysis of rice husk obtained from a biomass processing plant in Nanjing, China) was mixed thoroughly with 0.5 g of $Co(NO_3)_2{\cdot}6H_2O$ (Sigma-Aldrich, 99.999%). This mixture was then placed in a quartz boat and subjected to pre-carbonization in a tube furnace under Ar atmosphere. The temperature was increased at a heating rate of 5 °C/min until reaching 500 °C, and kept at that temperature for 1 hour. Subsequently, the mixture was cooled down naturally to room temperature and ground into powder. The pre-carbonized powder was further mixed with various ratios of NaOH (Aladdin, 98%), ground well, and placed in a clean alumina boat. The mixture was then subjected to carbonization in a tube furnace in Ar atmosphere, with the temperature increasing at a heating rate of 10 °C/min until reaching 800 °C, and held at that temperature for 2 hours. After cooling down naturally to room temperature, the resulting powder was fully ground into fine powder. The neutralization of the obtained powder was performed using 2 M HCl solution (Aladdin) to achieve a pH of 7. The product was then washed with distilled water to remove salts and impurities. Finally, the obtained sample was dried at 80 °C for 12 hours to obtain biochar. This biochar was named as Co-PB-*x*, where Co-PB represents the porous biochar prepared by co-catalytic pyrolysis, and *x* denotes the mass ratio of NaOH to the pre-carbonized product. The samples were further reduced in H_2 atmosphere at 500 °C. PB-*x* was also synthesized without the addition of $Co(NO_3)_2{\cdot}6H_2O$ at the initial stage, while keeping other steps constant.

Co-PB-3-IM (impregnation) was prepared using the impregnation method (IM). PB-3 was added to a solution of $Co(NO_3)_2{\cdot}6H_2O$ in a specific mass ratio and stirred for 3 hours at 60 °C. The resulting sample was incubated for a period of time and then dried at 100°C for 36 hours. Subsequently, it was calcined in Ar at 500 °C for 5 hours. Co-PB-3-IM was then reduced at 500°C in H_2 atmosphere.

Co-PB-3-DL (direct loading) was prepared using the direct loading method. The powders of PB-3 and $Co(NO_3)_2{\cdot}6H_2O$ were ball-milled at 500 rpm for 6 hours in a specific mass ratio. The samples were then reduced at 500 °C in H_2 atmosphere.

Catalyst characterization

X-ray diffraction (XRD) was used to analyze the crystal structure of the catalysts. XRD patterns of the catalysts were collected using a Bruker D2 Phaser with a Cu target, a voltage of 40 V and a current of 40 mA. X-ray photoelectron spectroscopy (XPS) was carried out on a Thermo Scientific ESCALAB Xi+ spectrometer, which utilizes an Al K_α X-ray (h_v=1486.65 eV) source with an energy of 30 eV and a power of 100 W (10 kV and 10 mA). The morphology of the samples was characterized using a scanning electron microscope (SEM, Hitachi Regulus 8100) and the elemental analyses of the samples were performed using an energy dispersive X-ray spectrometer (EDX) as an attachment to SEM instrument. Transmission electron microscopy (TEM) images of the samples were obtained using a FEI Talos F200x instrument. Fourier transform infrared (FT-IR) spectra were obtained on a Thermo Scientific Nicolet iS20 spectrometer. The Brunauer-Emmett-Teller (BET) surface area of the samples was determined by N_2 adsorption-desorption isotherms on a Micromeritics ASAP 2460 instrument. The samples were vacuum degassed for 8 hours at 150 °C prior to the BET test. Temperature-programmed desorption of ammonia (NH_3-TPD) was performed on a Micromeritics AutoChem II 2920. Co-PB-3 (100 mg) was dried from room temperature to 500 °C with a temperature ramp of 10 °C min^{-1}, then rinsed in 50 mL min^{-1} of pure He for 1 hour, and cooled to 50 °C. After purging in a gas mixture of 10% NH_3/He at a gas flow rate of 50 mL min^{-1} for 1 hour, the sample was replaced with pure He (50 mL min^{-1}) for 1 hour to remove the physically-adsorbed NH_3. The non-isothermal desorption of NH_3 was carried out in pure He at a heating rate of 10 °C min^{-1} over a temperature range of 50-800 °C.

Reaction apparatus and conditions

The dielectric barrier discharge (DBD) experimental setup is shown in Figure S1. The coaxial DBD reactor used in this experiment consists of a dielectric corundum tube with a length of 480 mm, an inner diameter of 10 mm and an outer diameter of 15 mm. A stainless steel rod with a length of 300 mm and a diameter of 5 mm was used as a high-voltage electrode, connected to a high-voltage power supply (CTP-2000K, 40 kHz, Nanjing Suman Electronics Co Ltd, Nanjing, China). The low-voltage electrode is a 200 mm long piece of externally wrapped stainless steel mesh that is

grounded to create a plasma discharge gap that is 2.5 mm wide and 200 mm long. The DBD reactor is heated by an externally wrapped tube furnace, and a fixed microporous substrate carries 0.1 g catalyst powder at the lowermost portion of the high-voltage electrode. The charge–voltage (Q–U) Lissajous curve calculation of output power is described in Supplementary Method 5 after the power supply is connected to an oscilloscope to obtain it. The corresponding circuit design is provided in Figure S11. H_2 and N_2 were supplied through a gas cylinder (Praxair, 99.99%), and the flow rate was controlled by a mass flow controller. The gas was well mixed before introducing into the DBD reactor. In general, if not otherwise specified, the reaction temperature was 200 °C, the N_2 and H_2 flow rates were both 50 ml min^{-1}, the plasma output power was 10 W, and the reaction rate was the average rate of the steady-state reaction for 3 hours. For the cycling experiments, each experiment was performed for 3 hours in the same reaction conditions as previously described. Afterwards, the samples were removed and placed in air for 3 hours before the next experiment.

RESULTS AND DISCUSSION

Preparation and characterization of Co-PB catalysts

The preparation process of Co-PB-*x* is shown in Figure 2A, where Co-PB represents the porous biochar obtained using the co-catalytic pyrolysis and *x* is the mass ratio of NaOH to the pre-carbonized product. During the pre-carbonization process, water and small molecules were removed from the heavy bio-oil, leading to an uniform distribution of Co in the product. In the secondary carbonization process, NaOH and Co act as activators, synergistically promoting the formation of the porous structure with three-dimensional interconnections. Moreover, for comparison, various biochar-based catalysts were also prepared by using different methods (see experimental section), such as PB-*x*, Co-PB-*x*-IM (impregnation) and Co-PB-*x*-DL (direct loading). It was found that the as-prepared catalysts presented different morphologies. Scanning electron microscope (SEM) image (Figure 2B) revealed a particle shape with nanoscale size for PB-3, and the accumulation of these particles formed numerous tiny holes and pores. In contrast, the pore structure of PB-1 is less dense, and the surface is relatively smooth (Figure S2). The Bruno-Emmett-Teller (BET, Table S1, Figure S3) result also indicates that the PB-3 has larger specific surface area, mainly attributed to the predominant pore-forming effect of NaOH, leading to an increase in specific surface area and total pore volume.[50] Figure 2C depicts the micro-structure of Co-PB-3-IM, which closely resembles with that of PB-3, indicating that the impregnation loading does not significantly alter the micro-structure of biochar.

As compared with other catalysts, the Co-PB-3 exhibits a more wrinkled and porous hollow structure (Figure 2D), which is beneficial for the reactions occurring on the catalyst. Moreover, the BET result reveals a larger specific surface area and hierarchical pore distribution (Figure S3). This unique structure can facilitate the process of gas mass transfer and increase the concentration of active site, and thus enhancing the performance of PAAS. The energy dispersive X-ray (EDX) elemental mapping of Co-PB-3 suggests a uniform distribution of Co in the support (Figure S4). The EDX spectra also indicated that the Na^+ and Cl^- species from the preparation process were completely washed out. Figure 2E shows the TEM images of Co-PB-3 with atomically resolved HR-TEM images along the directions of (111) and (200), displaying clear lattice fringes with spacing of 0.205 and 0.177 nm, respectively, which are in good accordance with the reference values of the XRD pattern for Co-PB-3 (Figure 2F). XRD patterns of Co-PB-3 and PB-3, revealed that no distinct characteristic peak of carbon was detected from both of them, suggesting a disordered structure of amorphous carbon that generally could give rise to an excellent porous structure and remarkable charge storage capacity.[48]

PAAS performance of the developed catalysts

To evaluate the PAAS performance of the as-prepared catalysts, a comprehensive evaluation was conducted (Figure 3A). Detailed information can be found in the reactor section of the experimental sections. The amount of the synthesized ammonia was measured by monitoring the change in conductivity of the absorption liquid (**Supplementary Method 1**). The accuracy of this conductivity method was verified by UV spectrophotometry (see Supplementary Method 6 and Figures S12–S13), and the deviation between the two methods was less than 1%, confirming the reliability of the conductivity-based NH_3 quantification. Results show that PB-1 exhibits the lowest ammonia synthesis rate, while a gradual improvement in the performance was obtained for PB-2 and PB-3, respectively, primarily attributed to the gradual enlargement of the pore structure and increase in the specific surface area, resulting in an enhancement on the gas transfer and adsorptive hydrogenation reactions.[51,52] However, PB-4 shows a decrease in performance due to the diminution in specific surface area of the porous carbon.

Overall, during the activation process, the generation of new micro-pores (pore opening) and the enlargement in pore size take place. The amount of activator used affects the activation reaction kinetics. Higher dosage of activator not only can lead to a more complete activation but also can increase the erosion of the activated carbon. When the activator dosage ratio is fewer than 3, the pore opening effect dominates, resulting in an increase in the specific surface area as well as the total pore volume. However, when the ratio is larger than 3, the pore expansion effect takes the dominant. Consequently, an excessive amount of NaOH leads to more severe erosion of the activated carbon. This erosion causes the collapse of the carbon skeleton around certain micro-pores, resulting in the transformation of some micro-pores into meso-pores or even macro-pores. As a result, the specific surface area and pore volume of the activated carbon continuously decrease.[48,50]

By adding the Co metal into biochar matrix, the PAAS performance is greatly improved. This is mainly due to that the transition metal can reduce the energy barrier of the surface hydrogenation-ammonia production reaction. Additionally, the utilization of a less nitrophilic metal-like Co favors the formation of intermediates and desorption of NH_3, suppressing the decomposition of ammonia, and thus breaking the linear relationship.[30,37] Compared to the direct loading (DL) of Co, the impregnation method (IM) leads to a more evenly distribution of Co, leading to the better PAAS performance of Co-PB-3-IM over Co-PB-3-DL.

By comparison, it can be found that the catalyst prepared by co-catalytic pyrolysis (Co-PB-3) shows much better performance than that of Co-PB-3-IM, which is most probably ascribed to the following factors. Firstly, the addition of cobalt nitrate during the initial stage ensures a more uniform distribution of Co and enhances the bonding between Co and C. The XPS results indicate that the Co-C bond was formed only during the co-catalytic pyrolysis (Figures. 3B & C, NIST XPS database), accelerating the charge transfer between Co and biochar, and thus improving its catalytic performance.[53,54] To get more information about the enhancement of the performance, the atomic migration on the surface of the catalyst and its synergistic mechanism were evaluated through density-functional theory (DFT) calculations as described in the **Supplementary Method 2**. The introduction of defects in the porous biochar increased the number of available valence electrons at the cavities, enabling stronger covalent bonding with the loaded clusters. Based on this (structure optimization is schematically shown in Figure S5), when comparing the processes of nitrogen fixation and hydrogenation for ammonia generation, Co-PB-3 exhibits a lower hydrogenation energy barrier, resulting in the improved PAAS performance (Figure 3D). To gain deeper insight into the reaction mechanism, we further discuss the possible plasma-induced reactive species and their roles in NH_3 formation. In the atmospheric-pressure DBD plasma, high-energy electrons collide with N_2 and H_2 molecules, generating a variety of reactive species including N atoms, H atoms, excited N_2, and NH_x (x = 1,2) radicals.[30,31] These gas-phase species can be adsorbed onto the catalyst surface, where they undergo successive hydrogenation steps to form NH_3. Our DFT calculations (Figure 3D) show that Co-PB-3 significantly lowers the energy barrier for key hydrogenation steps (e.g., N + H → NH), which is consistent with an Eley–Rideal type mechanism where gaseous or weakly adsorbed radicals react with surface-bound intermediates. The enhanced electron transfer between Co and the carbon support (Figures 3E & S6) likely facilitates the activation of adsorbed N_2 and the stabilization of NH_x intermediates, thereby promoting the overall conversion. According to the findings presented in Figures 3E & S6, it can be observed that there is an obvious occurrence of charge accumulation (yellow area) and charge reduction (cyan area) between the Co-cluster and the carbon substrate in Co-PB-3. This phenomenon suggests that a greater number of valence electrons from Co-clusters are transferred to the carbon substrate in Co-PB-3, leading to the formation of stronger chemical bonds between Co clusters and biochar.

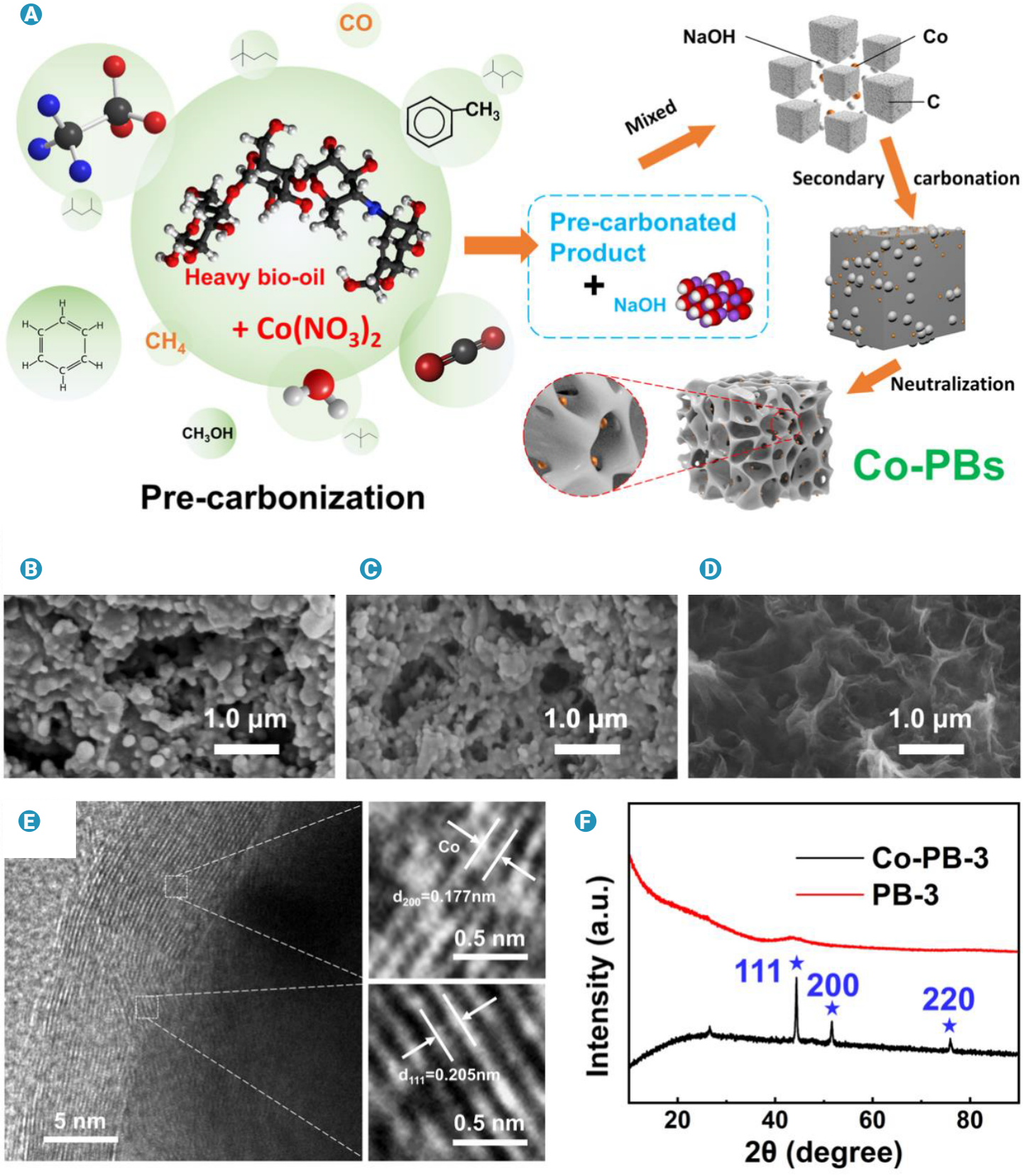

Figure 2. (A) Schematic plot of the route to fabricate Co-PB-x: Co-PB is the biochar obtained using co-catalytic pyrolysis with the addition of cobalt nitrate as catalyst. SEM images of the catalysts prepared from the different methods: (B) PB-3, (C) Co-PB-3-IM, (D) Co-PB-3; (E) TEM images of Co-PB-3; (F) XRD patterns of Co-PB-3 and PB-3.

Secondly, the FT-IR patterns in Figure 3F indicate a transition from the primary alcohol (R-CH_2-OH, 1034 cm^{-1}) in Co-PB-3-IM to the secondary alcohol (R-CH(R')-OH, 1126 cm^{-1}) in Co-PB-3. This implies that the co-catalytic pyrolysis method results in more alcohol groups being pyrolyzed, and further leading to the generation of more H adsorption sites. Consequently, the adsorption capacity for H radicals is greatly enhanced, thereby improving the PAAS performance of Co-PB-3.

Thirdly, the co-catalytic pyrolysis reduces the strength of the acidic centers

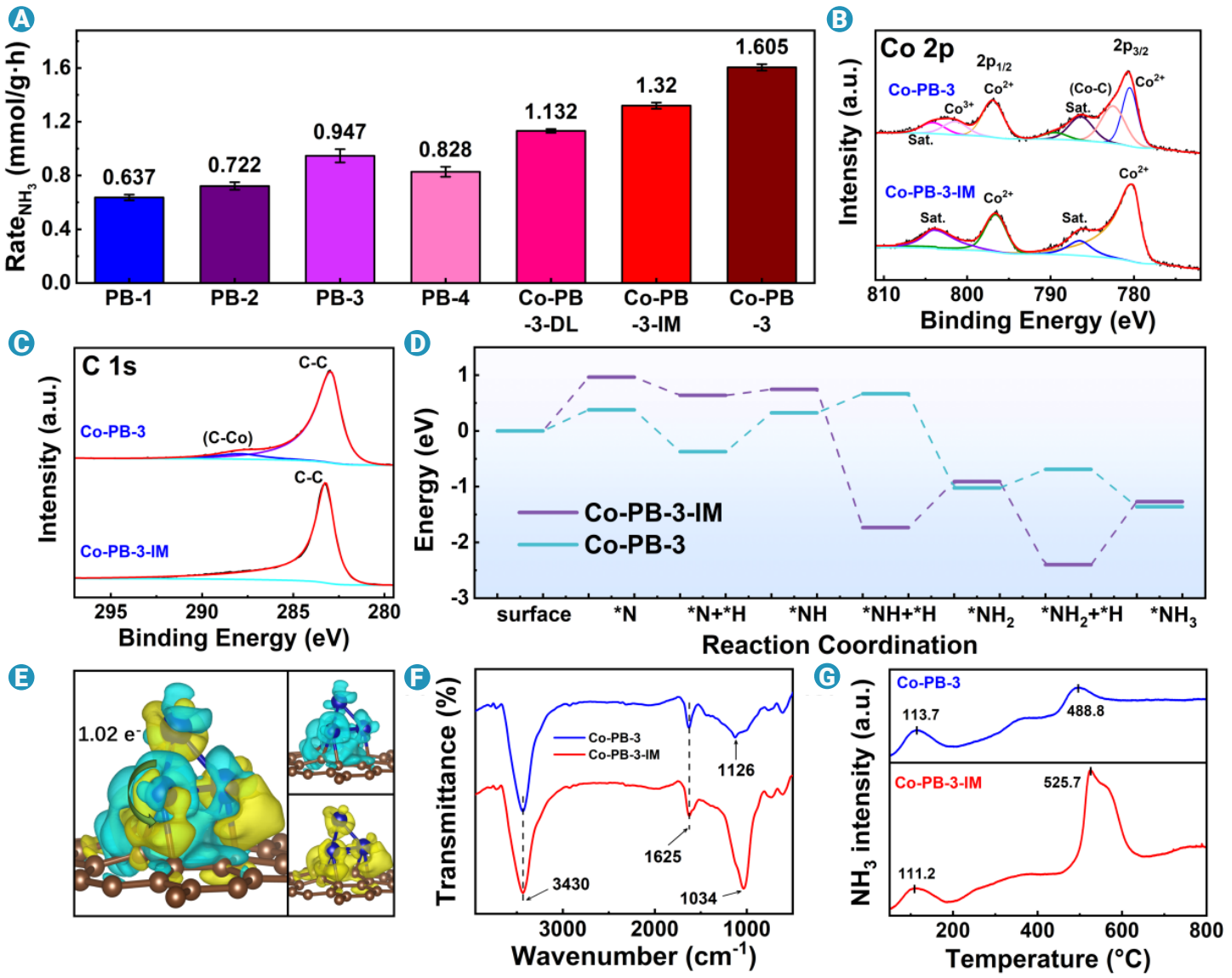

Figure 3. The PAAS performance of the different catalysts (A) Measured NH_3 synthesis rate of various catalysts: PB-1, PB-2, PB-3, PB-4, Co-PB-3-DL, Co-PB-3-IM and Co-PB-3. Note that the error bars represent the standard deviation of three parallel tests. XPS spectra of Co-PB-3 and Co-PB-3-IM: (B) Co 2p, and (C) C 1s. (D) DFT calculations of the reaction pathway of PAAS on Co-PB-3-IM and Co-PB-3. (E) Charge differential density plot of Co-PB-3. (F) FTIR spectra of Co-PB-3. (G) NH_3-TPD profiles of Co-PB-3 and Co-PB-3-IM.

on the catalyst surface, which facilitates the process of ammonia desorption. The NH_3-TPD profiles (Figure 3G) show the chemical desorption peaks of NH_3 at different acidic sites, and the acidity of these sites is listed in Table S2. The total number of acidic sites in Co-PB-3 (0.499 mmol g^{-1}) is significantly lower than that in Co-PB-3-IM (0.950 mmol g^{-1}), showing a substantial reduction in strongly acidic sites. This reduction not only favors the desorption of the generated NH_3 from the catalyst's surface, but also inhibits the decomposition of ammonia on the catalyst's surface. Fourthly, Co-PB-3 displays the improved performance of electric field characteristics, as indicated by the increased area of the Lissajous graphs under constant inputs (Figure S7). This increase correlates with the prominent improvement in the discharge efficiency of Co-PB-3.

Lastly, numerical simulations based on finite element analysis (FEA) were conducted to investigate the mass transfer characteristics of Co-PB-3 and Co-PB-3-IM (**Supplementary Method 3**), as depicted in Figures 4A-D. The average mass transfer rates (Figure S8) indicate that the transfer rates of gas radicals in Co-PB-3 are considerably higher than those in Co-PB-3-IM. This difference can be attributed solely to the distinct micro-pore structures of the two catalysts. The enhanced gas radical transfer of Co-PB-3 enables a greater number of radicals to interact with the active sites. Additionally, it facilitates more gas radicals to react within the small discharge gaps of the catalyst particles, consequently leading to the improved PAAS performance.

To further understand the mechanism of PAAS, we conducted experiments to measure the ammonia synthesis rate at different ratios of H_2/N_2 (Figure 4E). Results show that the optimum ratio of H_2/N_2 for the PAAS reaction is 1:1, which is consistent with several recent reports that also found the optimal ratio to be non stoichiometric (e.g., 1:1 or 2:1) because of the easier dissociation of H_2 compared to that of N_2 in plasma.[26,55-59] In the theoretical reaction, NH_3 is formed from H_2 and N_2 according to the equation $3H_2 + N_2 \rightarrow 2NH_3$, resulting in a stoichiometric ratio of 3:1. However, the decisive step limiting the reaction rate is the dissociation of N≡N (945.6 kJ·mol^{-1}), which is much more difficult than that of H–H (391.0 kJ·mol^{-1}). Consequently, the dissociation percentage of N_2 is lower than that of H_2 under the same plasma discharge power. This necessitates a higher proportion of N_2 in the feed to balance the generation of N and H radicals, leading to an optimal H_2/N_2 ratio of around 1:1.

Figure 4F illustrates the impact of temperature on the PAAS performance. In the absence of catalyst, the PAAS rate remains relatively constant regardless of the temperature. This is attributed to the absence of non-homogeneous surface reactions but the predominant presence of homogeneous plasma phase reactions, which are independent on the temperature change. However, for catalysts such as PB-3, Co-PB-3-IM, and Co-PB-3, increasing

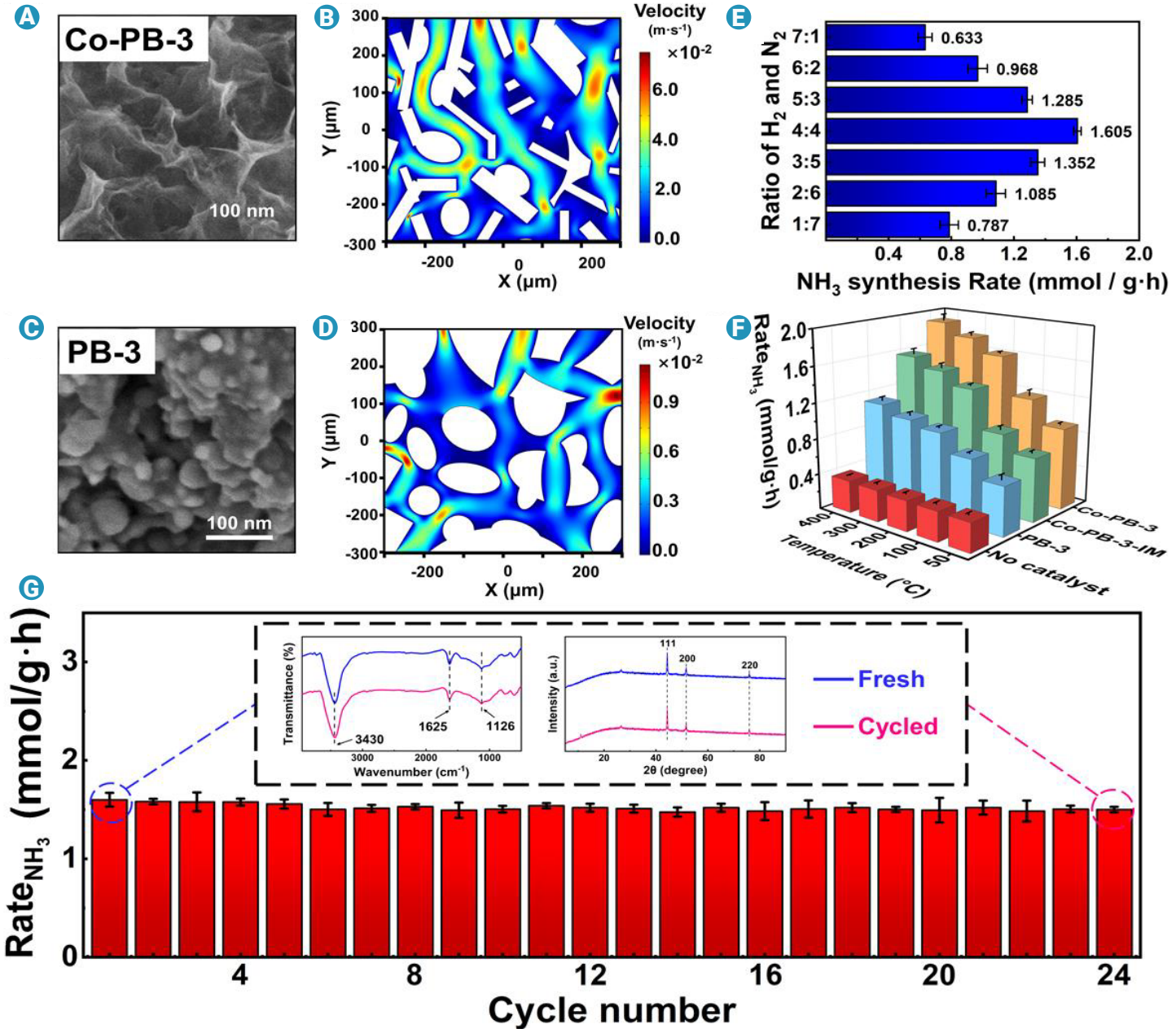

Figure 4. SEM images and gas radical transport performance of (A&B) Co-PB-3, and (C&D) Co-PB-3-IM. PAAS rates are shown as a function of (E) the ratio of H_2 and N_2, and (F) temperature. (G) Cyclic tests of Co-PB-3. Inserts show the FTIR spectra and XRD patterns of Co-PB-3 before and after the cyclic PAAS reactions. For each experiment, standard conditions were applied except for the dependent variable.

the temperature enhances the performance of PAAS. This is because higher temperature promotes the non-homogeneous phase reaction on the catalyst's surface, and therefore enhances the surface hydrogenation for ammonia production. Furthermore, the increased temperature accelerates the desorption process of NH_3 generated by the reaction on the catalyst's surface. This greatly reduces the impact of ammonia decomposition and results in an increased rate of ammonia synthesis.[60] A more in-depth analysis of the temperature effect on PAAS can be understood from the following perspectives. First, although NH_3 synthesis is an exothermic reaction and lower temperatures favor higher equilibrium yields, the PAAS process is kinetically controlled. At low temperatures (<300 °C), NH_3 synthesis is primarily attributed to the adsorption of plasma-generated N radicals and their subsequent hydrogenation, a kinetically dominated process rather than one constrained by thermodynamic equilibrium.[33] Therefore, the observed increase in synthesis rate with temperature in the range of 50–200 °C is entirely consistent with kinetic principles. Second, the elevated temperature accelerates surface hydrogenation reactions (Arrhenius behavior). For Co-PB-3, this effect is more pronounced because the Co–C covalent bonding facilitates electron transfer from Co to the carbon support (Figures 3E & S6) and lowers the energy barriers for key hydrogenation steps (Figure 3D), making the surface hydrogenation more temperature-sensitive. Third, the elevated temperature has been shown to promote NH_3 desorption from the catalyst surface, alleviating product inhibition and exposing more active sites for further N_2 activation and hydrogenation.

It is important to note that the N≡N bond dissociation still relies on high-energy electrons from the plasma, not on thermal activation. Temperature therefore acts as a kinetic modulator rather than a direct driver of N_2 activation, and the observed synergy between plasma and Co-PB-3 is primarily manifested through temperature-enhanced surface hydrogenation and desorption steps.

As the total gas flow rate rises, the PAAS rate also improves, especially at lower total gas flow rates (Figure S9). It is apparently a result of the increase in the number of radicals as the total gas flow rate grows. The slower increase of PAAS rate at higher total gas flow rates is caused by, on the one

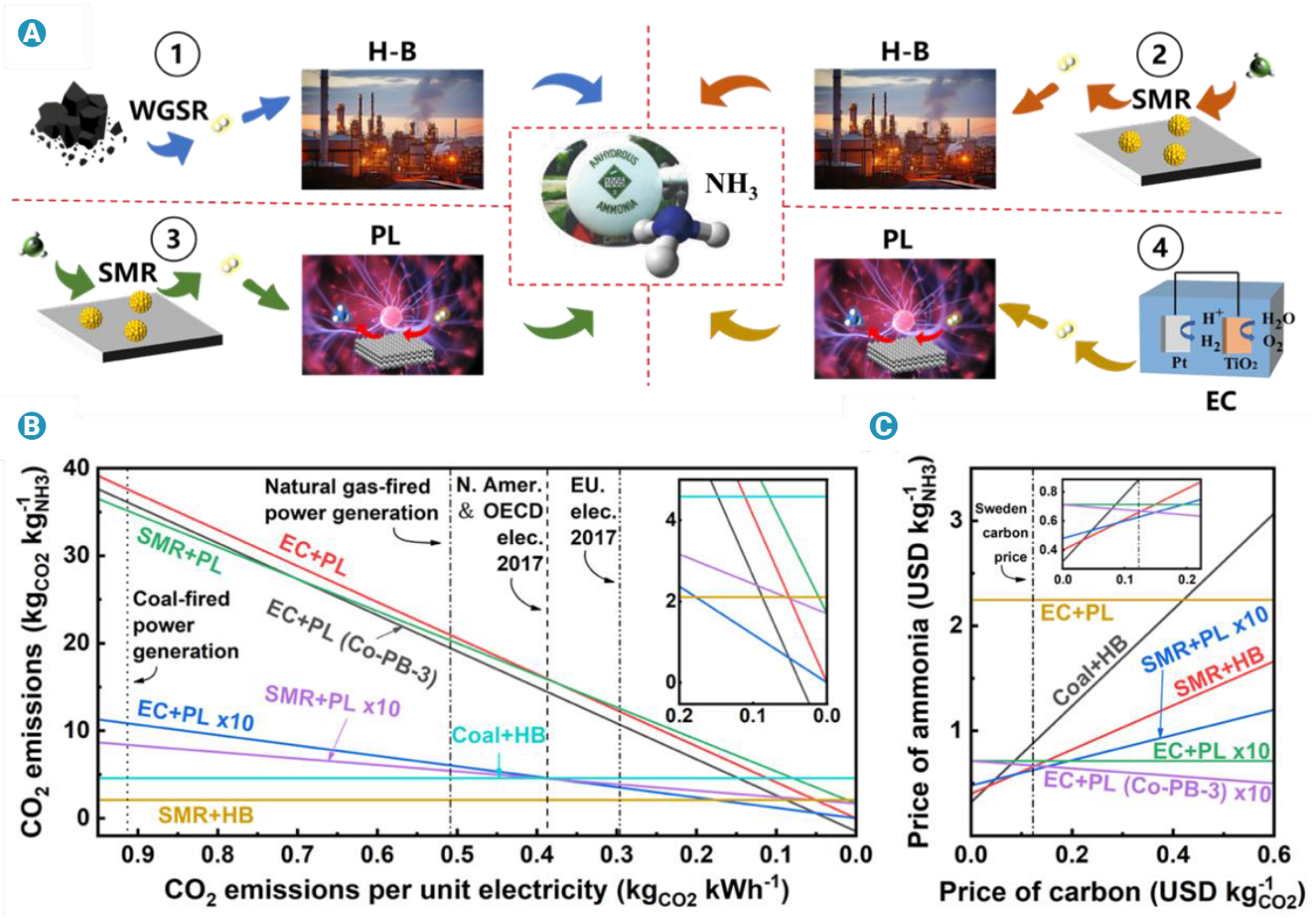

Figure 5. Environmental and economic competitiveness analysis of PAAS (A) Schemes of different technologies of hydrogen and ammonia synthesis: ① water-gas shift reaction of coal (WGSR) for H_2 production and H-B for ammonia synthesis; ② reforming of methane (SMR) for H_2 production and H-B for ammonia synthesis; ③ SMR for H_2 production and PAAS (PL) for ammonia synthesis; ④electrolysis of water (EC) for H_2 production and PL for ammonia synthesis. (B) Carbon emission of different ammonia synthesis technology using different electricity as power (different CO_2 emission per unit electricity). (C) Ammonia price of different ammonia synthesis technology based on carbon price.

hand, the limited plasma output power that gradually reduces the proportion of the dissociated gas. On the other hand, the higher gas flow rate may induce a reduction of the PAAS rate because of the energy loss as more radicals are removed by the newly introduced gas before they can participate in the reaction in time.

To evaluate the cycling performance of Co-PB-3, we conducted a series of tests over 24 cycles (Figure 4G). The PAAS performance shows a very slight decline after the 6th cycle, which could be attributed to the occupation of some active sites by free radicals. However, the performance remains stable thereafter. To determine the impact of plasma discharge on the surface functional groups and crystalline phase structure of Co-PB-3, we analyzed the FTIR spectra and XRD patterns before and after the cyclic

reactions (inset images of Figure 4G). The results reveal that the FTIR spectra and XRD patterns are almost identical: all characteristic peaks show no shift, and no new peaks indicative of structural collapse or metal aggregation were detected, indicating that the plasma discharge does not affect the surface and crystal structure. Furthermore, the PAAS performance of Co-PB-3 remains steady throughout the 40 hours reaction (Figure S10). In summary, Co-PB-3 demonstrates a tendency to maintain its original structure and shows good stability during the cycling experiments, making it a potential candidate for the industrial decentralized ammonia production.

Although we cannot directly quantify the fraction of electrons contributing to N_2 activation at this stage, several lines of indirect evidence suggest the improved electron utilization efficiency on Co-PB-3. First, the Lissajous curves (Figure S7) show that Co-PB-3 exhibits a larger discharge area than that of Co-PB-3-IM under the same input power, indicating a higher discharge power and thus a greater number of high-energy electrons available for molecular activation. Second, the charge differential density analysis (Figures 3E & S6) reveals the stronger electron transfer from the Co clusters to the carbon substrate in Co-PB-3, which facilitates the electron donation to the adsorbed N_2 and N-containing intermediates. These observations collectively imply that Co-PB-3 enables more efficient use of plasma-generated electrons for N_2 activation. Future work using in situ optical emission spectroscopy (OES) with actinometry will be pursued to quantitatively determine the electron energy utilization efficiency.

To highlight the superiority of the developed Co-PB-3 catalyst, the energy efficiency is also compared with the reported data. Using the measured discharge power (10 W, from Lissajous analysis, Supplementary Method 5) and the NH_3 synthesis rate over Co-PB-3 (1.605 $mmol \cdot g^{-1} \cdot h^{-1}$, Figure 3A), the energy yield (EY) is calculated to be 2.73 g-NH_3/kWh (0.0446 mmol/kJ). The specific energy input (SEI) under the typical conditions (total flow of 100 mL/min, discharge power of 10 W) is 6 kJ/L and the steady-state NH_3 concentration is ~6550 ppm (vol/vol). Compared with typical DBD plasma-catalytic systems reported in the literature (e.g., Ni/Al_2O_3 ~0.3–0.5 g/kWh, Co-MOF ~0.4–0.6 g/kWh), the energy yield of Co-PB-3 is competitive.[42,61]

Supplementary experiments with different catalyst loadings (100–200 mg) revealed an optimal loading of 150 mg, giving an NH_3 synthesis rate of 2438 $\mu mol \cdot g^{-1} \cdot h^{-1}$, which is even higher than the rate obtained with 100 mg loading (see Table S6).

Economic and environmental analysis of different ammonia synthesis processes

To evaluate the technical and economic feasibility of PAAS, we carefully carry out an analysis on the competitiveness of ammonia synthesis using plasma nitrogen fixation in terms of CO_2 emissions and costs.[62] Four different routines including both H-B and PAAS processes for ammonia synthesis were taken into account for a systematic comparison, as illustrated in Figure 5A. The feeding hydrogen is generated by using different technologies, such as Water-Gas Shift Reaction of coal (WGSR), Steam Reforming of methane (SMR), and electrolysis of water (EC). In Figure 5B, we present the overall carbon emission of various technological options, considering their variation with the carbon emission per unit of electricity generated. Here, the 'H-B process' benchmark refers to the SMR+HB route (H_2 from steam methane reforming followed by the Haber-Bosch process; see Figure 5A for all four routes). The detailed implications and calculations can be found in Supplementary Method 4 and Tables S3-S5. Currently, if using the fossil fuel-based electricity, the carbon emission of PAAS in our lab scale is not competitive compared with that of the H-B process, using either SMR or EC for hydrogen production. However, if the PAAS rate is maintained within a 10-fold increase in catalyst amount, its environmental friendliness will be able to compete with that of the H-B process utilizing coal (average carbon emissions for North American and OECD electricity in 2017).[63] Additionally, when the electricity is primarily sourced from CO_2-free renewable sources like solar and wind (<0.05 $kg_{co_2} kWh^{-1}$), the carbon emission will be comparable to that of SMR + HB, without consuming fossil fuels (as shown in the inserted figure in Figure 5B). Moreover, by considering the economic and environmental cost savings achieved in the catalyst preparation process using heavy bio-oil, the carbon emission can be further reduced below those of the H-B process with WGSR or SMR.

Figure 5C presents a preliminary assessment of the economic competitiveness of the PAAS process. The analysis aims to evaluate the potential of PAAS plants for industrial applications under ideal conditions, with a simplified approach that does not consider investment costs, chains, and specific steps. Without factoring in the cost of carbon (carbon price is 0), the PAAS process is currently not competitive compared to the H-B process. However, as environmental awareness continues to grow, the environmental and economic competitiveness of the PAAS process is improving. Considering the carbon price in Sweden, the 10-fold enhanced PAAS with SMR process can already compete with the H-B process. In the future, as the carbon price increases, the economy of the PAAS process will surpass that of the H-B process, indicating its full capability to compete at this stage. In short, the small-scale and distributed PAAS plant, powered entirely by renewable electricity, is highly attractive considering the global trend towards carbon neutrality. Moreover, the PAAS also provides an efficient alternative for renewable energy storage in the remote area, such as mountainous solar power and off-shore wind power.

CONCLUSION

In conclusion, we have successfully developed a cascade porous biochar-based metal catalyst from the waste heavy bio-oil for PAAS by using a simple co-catalytic pyrolysis method. This method eliminates the energy consumption in the metal loading process for the PAAS catalysts. Co acts as pyrolysis catalyst, causing a reconfiguration of the micro-morphology to form a more sparse and porous hollow carbon skeleton structure. Meanwhile, it also acts as active site for PAAS, enhancing the ammonia synthesis performance. The improved performance can be primarily attributed to the enhanced mass transfer kinetics, resulting from the loose and porous structure. Furthermore, the co-catalytic pyrolysis process leads to a more uniform distribution of the metal and reduces the strength of the surface acidic sites, facilitating the synthesis and desorption of NH_3. The catalyst, Co-PB-3, exhibits excellent stability and cycling performance, maintaining its structure and performance for a flow period of up to 40 h and 24 cycles. This study demonstrates the significant potential of this porous biochar-based metal material as an effective catalyst in the field of PAAS, paving a new avenue for electricity and hydrogen storage. These findings provide a promising approach for the industrial application of PAAS and highlight its feasibility as a future alternative for zero-carbon ammonia synthesis process.

REFERENCES

1. Chai W. S., Bao Y., Jin P., et al. (2021). A review on ammonia, ammonia-hydrogen and ammonia-methane fuels. *Renew. Sustain. Energy Rev.* **147**:111254. DOI:10.1016/j.rser.2021.111254
2. MacFarlane D. R., Cherepanov P. V., Choi J., et al. (2020). A Roadmap to the Ammonia Economy. *Joule* **4**:1186–1205. DOI:10.1016/j.joule.2020.04.004
3. Aziz M., Wijayanta A. T. and Nandiyanto A. B. D. (2020). Ammonia as Effective Hydrogen Storage: A Review on Production, Storage and Utilization. *Energies* **13**:3062. DOI:10.3390/en13123062
4. Lamb K. E., Dolan M. D. and Kennedy D. F. (2019). Ammonia for hydrogen storage; A review of catalytic ammonia decomposition and hydrogen separation and purification. *Int. J. Hydr. Energy* **44**:3580–3593. DOI:10.1016/j.ijhydene.2018.12.024
5. Lan R., Irvine J. T. S. and Tao S. (2012). Ammonia and related chemicals as potential indirect hydrogen storage materials. *Int. J. Hydro. Energy* **37**:1482–1494. DOI:10.1016/j.ijhydene.2011.10.004
6. Kandemir T., Schuster M. E., Senyshyn A., et al. (2013). The Haber-Bosch process revisited: on the real structure and stability of "ammonia iron" under working conditions. *Angew. Chem. Int. Ed. Engl.* **52**:12723–12726. DOI:10.1002/anie.201305812
7. Lan R., Irvine J. T. and Tao S. (2013). Synthesis of ammonia directly from air and water at ambient temperature and pressure. *Sci. Rep.* **3**:1145. DOI:10.1038/srep01145
8. Rohr B. A., Singh A. R. and Nørskov J. K. (2019). A theoretical explanation of the effect of oxygen poisoning on industrial Haber-Bosch catalysts. *J. Catal.* **372**:33–38. DOI:10.1016/j.jcat.2019.01.042
9. Vojvodic A., Medford A. J., Studt F., et al. (2014). Exploring the limits: A low-pressure, low-temperature Haber–Bosch process. *Chem. Phys. Lett.* **598**:108–112. DOI:10.1016/j.cplett.2014.03.003
10. Lee K., Liu X., Vyawahare P., et al. (2022). Techno-economic performances and life cycle greenhouse gas emissions of various ammonia production pathways including conventional, carbon-capturing, nuclear-powered, and renewable production. *Green Chem.* **24**:4830–4844. DOI:10.1039/d2gc00843b
11. Zhou Q., Gong F., Xie Y., et al. (2022). 1+1>2: Learning from the interfacial modulation on single-atom electrocatalysts to design dual-atom electrocatalysts for dinitrogen reduction. *Green Energy Environ.* DOI: 10.1016/j.gee.2022.1006.1005. DOI:10.1016/j.gee.2022.06.005
12. Bo Y., Wang H., Lin Y., et al. (2021). Altering Hydrogenation Pathways in Photocatalytic Nitrogen Fixation by Tuning Local Electronic Structure of Oxygen Vacancy with Dopant. *Angew. Chem. Int. Ed. Engl.* **60**:16085–16092. DOI:10.1002/anie.202104001
13. Dong G., Ho W. and Wang C. (2015). Selective photocatalytic N2 fixation dependent on g-C3N4 induced by nitrogen vacancies. *J. Mater. Chem. A* **3**:23435–23441. DOI:10.1039/c5ta06540b
14. Li P., Zhou Z., Wang Q., et al. (2020). Visible-Light-Driven Nitrogen Fixation Catalyzed by Bi(5)O(7)Br Nanostructures: Enhanced Performance by Oxygen Vacancies. *J. Am. Chem. Soc.* **142**:12430–12439. DOI:10.1021/jacs.0c05097
15. Giddey S., Badwal S. P. S. and Kulkarni A. (2013). Review of electrochemical ammonia production technologies and materials. *Int. J. Hydro. Energy* **38**:14576–14594. DOI:10.1016/j.ijhydene.2013.09.054
16. Yang B., Ding W., Zhang H., et al. (2021). Recent progress in electrochemical synthesis of ammonia from nitrogen: strategies to improve the catalytic activity and selectivity. *Energy Environ. Sci.* **14**:672–687. DOI:10.1039/d0ee02263b
17. Liu X., Liu C., He X., et al. (2024). Fe-doped Co3O4 nanowire strutted 3D pinewood-derived carbon: A highly selective electrocatalyst for ammonia production via nitrate reduction. *Nano Res.* **17**:2276–2282. DOI:10.1007/s12274-023-6204-y
18. Wang S., Gong F., Zhou Q., et al. (2023). Transition metal enhanced chromium nitride as composite nitrogen carrier for sustainable chemical looping ammonia synthesis. *Appl. Cata. B Environ.* 339. DOI:10.1016/j.apcatb.2023.123134
19. Fu E., Gong F., Wang S., et al. (2023). Ni-Mn-N derived composite nitrogen carriers for enhanced chemical looping ammonia production. *Fuel Process. Tech.* 252. DOI:10.1016/j.fuproc.2023.107971
20. Gao W., Guo J., Wang P., et al. (2018). Production of ammonia via a chemical looping process based on metal imides as nitrogen carriers. *Nat. Energy* **3**:1067–1075. DOI:10.1038/s41560-018-0268-z
21. Feng J., Gong F., Liu C., et al. (2024). Self-assembled chromium-based nitrogen carrier for chemical looping ammonia synthesis. *Int. J. Hydrogen Energy* 83:491-498. DOI:https://doi.org/10.1016/j.ijhydene.2024.08.127
22. Mahmud K., Makaju S., Ibrahim R., et al. (2020). Current Progress in Nitrogen Fixing Plants and Microbiome Research. *Plants (Basel)* **9**:97. DOI:10.3390/plants9010097
23. Mus F., Crook M. B., Garcia K., et al. (2016). Symbiotic Nitrogen Fixation and the Challenges to Its Extension to Nonlegumes. *Appl. Environ. Microbiol.* **82**:3698–3710. DOI:10.1128/AEM.01055-16
24. Wang W. L., Moore J. K., Martiny A. C., et al. (2019). Convergent estimates of marine nitrogen fixation. *Nature* **566**:205–211. DOI:10.1038/s41586-019-0911-2
25. Ganji P., Zaplotnik R., Primc G., et al. (2025). Roles of Catalysts in Plasma Conversion of N2 and H2 to NH3: Advances, Challenges, and Future Directions. *Energy Fuels* **39**:14413–14436. DOI:10.1021/acs.energyfuels.5c01891
26. Gao B., Cao G., Hu D., et al. (2025). Insight into the effect of support properties on

DBD plasma-catalytic NH3 synthesis over Ru-Co bimetallic catalysts. *Fuel* 382:133802. DOI:10.1016/j.fuel.2024.133802
27. Lu B., Sun S. and Qiu H. (2025). Exploring the Origin of Synergistic Effect in Plasma-Assisted Ammonia Synthesis over a Ni Catalyst. *Langmuir* **41**:13119–13125. DOI:10.1021/acs.langmuir.5c00745
28. Wang Z., Gong F., Zhang L., et al. (2019). Electrocatalytic Hydrogenation of N2 to NH3 by MnO: Experimental and Theoretical Investigations. *Adv. Sci.* **6**:1801182. DOI. DOI:10.1002/advs.201801182
29. Yang P., Gong F., Liu C., et al. (2024). Mechanistic insights into the stepwise lithium-mediated electrochemical nitrogen reduction for enhanced ammonia synthesis. *Chem. Eng. J.* 488:151098. DOI:https://doi.org/10.1016/j.cej.2024.151098.
30. Mehta P., Barboun P., Herrera F. A., et al. (2018). Overcoming ammonia synthesis scaling relations with plasma-enabled catalysis. *Nat. Catal.* **1**:269–275. DOI:10.1038/s41929-018-0045-1
31. Wang Y., Craven M., Yu X., et al. (2019). Plasma-Enhanced Catalytic Synthesis of Ammonia over a Ni/Al(2)O(3) Catalyst at Near-Room Temperature: Insights into the Importance of the Catalyst Surface on the Reaction Mechanism. *ACS Cata.* **9**:10780–10793. DOI:10.1021/acscatal.9b02538
32. Zhao H., Song G., Chen Z., et al. (2021). In Situ Identification of NNH and N2H2 by Using Molecular-Beam Mass Spectrometry in Plasma-Assisted Catalysis for NH3 Synthesis. *ACS Energy Lett.* **7**:53–58. DOI:10.1021/acsenergylett.1c02207
33. Rouwenhorst K. H. R., Kim H.-H. and Lefferts L. (2019). Vibrationally Excited Activation of N2 in Plasma-Enhanced Catalytic Ammonia Synthesis: A Kinetic Analysis. *ACS Sustain. Chem. Eng.* **7**:17515–17522. DOI:10.1021/acssuschemeng.9b04997
34. Barboun P., Mehta P., Herrera F. A., et al. (2019). Distinguishing Plasma Contributions to Catalyst Performance in Plasma-Assisted Ammonia Synthesis. *ACS Sustain. Chem. Eng.* **7**:8621–8630. DOI:10.1021/acssuschemeng.9b00406
35. Bogaerts A. and Neyts E. C. (2018). Plasma Technology: An Emerging Technology for Energy Storage. *ACS Energy Lett.* **3**:1013–1027. DOI:10.1021/acsenergylett.8b00184
36. Winter L. R., Ashford B., Hong J., et al. (2020). Identifying Surface Reaction Intermediates in Plasma Catalytic Ammonia Synthesis. *ACS Cata.* **10**:14763–14774. DOI:10.1021/acscatal.0c03166
37. Liu T.-W., Gorky F., Carreon M. L., et al. (2022). Energetics of Reaction Pathways Enabled by N and H Radicals during Catalytic, Plasma-Assisted NH3 Synthesis. *ACS Sustain. Chem. Eng.* **10**:2034–2051. DOI:10.1021/acssuschemeng.1c05660
38. Chen Z., Koel B. E. and Sundaresan S. (2021). Plasma-assisted catalysis for ammonia synthesis in a dielectric barrier discharge reactor: key surface reaction steps and potential causes of low energy yield. *J. Phys. D Appl. Phys.* **55**:055202. DOI:10.1088/1361-6463/ac2f12
39. Liu J., Zhu X., Hu X., et al. (2022). Plasma-assisted ammonia synthesis in a packed-bed dielectric barrier discharge reactor: roles of dielectric constant and thermal conductivity of packing materials. *Plasma Sci. Tech.* 24. DOI:10.1088/2058-6272/ac39fb
40. Gorky F., Guthrie S. R., Smoljan C. S., et al. (2021). Plasma ammonia synthesis over mesoporous silica SBA-15. *J. Phys. D Appl. Phys.* 54. DOI:10.1088/1361-6463/abefbc
41. Gorky F., Lucero J. M., Crawford J. M., et al. (2021). Plasma-Induced Catalytic Conversion of Nitrogen and Hydrogen to Ammonia over Zeolitic Imidazolate Frameworks ZIF-8 and ZIF-67. *ACS Appl. Mater. Interfaces* **13**:21338–21348. DOI:10.1021/acsami.1c03115
42. Jing Y., Gong F., Wang S., et al. (2024). Activating the synergistic effect in Ni-Co bimetallic MOF for enhanced plasma-assisted ammonia synthesis. *Fuel* **368**:131686. DOI:10.1016/j.fuel.2024.131686
43. Shah J., Wu T., Lucero J., et al. (2018). Nonthermal Plasma Synthesis of Ammonia over Ni-MOF-74. *ACS Sustain. Chem. Eng.* **7**:377–383. DOI:10.1021/acssuschemeng.8b03705
44. Zhang Z., Wang Y., Guo T., et al. (2025). The Influence of Defect Engineering on the Electronic Structure of Active Centers on the Catalyst Surface. *Catalysts*. DOI:10.3390/catal15070651
45. Clarke R. J., Nice I. J. and Hicks J. C. (2025). Plasma-Catalyst Dynamics: Nonthermal Activation of Strong Metal–Support Interactions. *J. Ame. Chem. Soc.* **147**:585–593. DOI:10.1021/jacs.4c12388
46. Bajpai A. and Kumar S. (2024). Tailoring the surface acidity of catalyst to enhance nonthermal plasma-assisted ammonia synthesis rates. *Mole. Cata.* **557**:113961. DOI:10.1016/j.mcat.2024.113961
47. Hu X., Zhu X., Wu X., et al. (2020). Plasma-enhanced NH3 synthesis over activated carbon-based catalysts: Effect of active metal phase. *Plasma Proces. Poly.* **17**:2000072. DOI:10.1002/ppap.202000072
48. Zhu Y., Li Z., Tao Y., et al. (2022). Hierarchical porous carbon materials produced from heavy bio-oil for high-performance supercapacitor electrodes. *J. Energy Storage* 47. DOI:10.1016/j.est.2021.103624
49. Xu J., Xue B., Liu C., et al. (2021). Efficient utilization of crude bio-oil: the synthesis of nitrogen-doped hierarchically porous carbon as electrocatalysts for the oxygen reduction reaction. *Sustain. Energy Fuels* **5**:3884–3894. DOI:10.1039/d1se00652e
50. Wu C., Xu J., Ding J., et al. (2016). High-Performance Supercapacitor Based on the NaOH Activated D-Glucose Derived Carbon. *Nano* 11. DOI:10.1142/s1793292016500752
51. Navascués P., Obrero-Pérez J. M., Cotrino J., et al. (2020). Unraveling Discharge and Surface Mechanisms in Plasma-Assisted Ammonia Reactions. *ACS Sustain. Chem. Eng.* **8**:14855–14866. DOI:10.1021/acssuschemeng.0c04461
52. Neyts E. C., Ostrikov K. K., Sunkara M. K., et al. (2015). Plasma Catalysis: Synergistic Effects at the Nanoscale. *Chem. Rev.* **115**:13408–13446. DOI:10.1021/acs.chemrev.5b00362
53. Debalina B., Reddy R. B. and Vinu R. (2017). Production of carbon nanostructures in biochar, bio-oil and gases from bagasse via microwave assisted pyrolysis using Fe and Co as susceptors. *J. Anal. Appl. Pyro.* **124**:310–318. DOI:10.1016/j.jaap.2017.01.018
54. Qiu W., Liu Y., Tian L., et al. (2023). Cobalt-supported activated biochar in the co-pyrolysis of cattle manure and rice husk. *Proceed. Ins. Civil Eng. Energy*:1-10. DOI:10.1680/jener.23.00014
55. Zhu X., Hu X., Wu X., et al. (2020). Ammonia synthesis over γ-Al2O3 pellets in a packed-bed dielectric barrier discharge reactor. *J. Phy. D Appl. Phys.* 53. DOI:10.1088/1361-6463/ab6cd1
56. Rouwenhorst K. H. R., Mani S. and Lefferts L. (2022). Improving the Energy Yield of Plasma-Based Ammonia Synthesis with In Situ Adsorption. *ACS Sustain. Chem. Eng.* **10**:1994–2000. DOI:10.1021/acssuschemeng.1c08467
57. Hosseini H. (2023). Dielectric barrier discharge plasma catalysis as an alternative approach for the synthesis of ammonia: a review. *RSC Adv.* **13**:28211–28223. DOI:10.1039/D3RA05580A
58. Feng Y., Gao B., Cao G., et al. (2025). Co-doping facilitated plasma-catalytic ammonia synthesis over Mo2N-Co catalysts. *Front. Chem. Sci. Eng.* **19**:83. DOI:10.1007/s11705-025-2595-5
59. Wang Y., Yang W., Xu S., et al. (2022). Shielding Protection by Mesoporous Catalysts for Improving Plasma-Catalytic Ambient Ammonia Synthesis. *J. Ame. Chem. Soc.* **144**:12020–12031. DOI:10.1021/jacs.2c01950
60. Liu Y., Wang C. W., Xu X. F., et al. (2022). Synergistic Effect of Co–Ni Bimetal on Plasma Catalytic Ammonia Synthesis. *Plasma Chemistry and Plasma Processing* **42**:267–282. DOI:10.1007/s11090-021-10223-1
61. Zhou G., Zhao H., Wang X., et al. (2024). Plasma-catalytic ammonia synthesis on Ni catalysts supported on Al2O3, Si-MCM-41 and SiO2. *Int. J. Hydro. Energy* **60**:802–813. DOI:10.1016/j.ijhydene.2024.02.200
62. Winter L. R. and Chen J. G. (2021). N2 Fixation by Plasma-Activated Processes. *Joule* **5**:300–315. DOI:10.1016/j.joule.2020.11.009
63. IEA(2019) (2019). CO2 Emissions from Fuel Combustion (OECD Publishing).

FUNDING AND ACKNOWLEDGMENTS

The authors would like to thank the financial support from the Open Project Program of State Key Laboratory of Low-carbon Smart Coal-fired Power Generation and Ultra-clean Emission (grant number D2024FK144) and the Science and Technology Department of Jiangsu Province (BZ2024033, BT2024006). The modeling and DFT calculations are supported by the Big Data Computing Center of Southeast University.

AUTHOR CONTRIBUTIONS

All authors have made substantial contributions to this work and approved the final manuscript. F. Gong: Conceptualization, Funding acquisition, Project administration, Supervision, Writing - original draft, Writing - review & editing. J. Bao: Methodology, Investigation, Formal analysis, Validation, Data curation, Writing original draft. Y. Jing:Investigation, Validation, Data curation. Q. Zhou: DFT calculations, Formal analysis, Writing - review & editing. C. Liu: Finite element simulation, Methodology. S. Hong: Catalyst characterization, Investigation. Z. Zhang: Experimental assistance, Data collection. W. Fan: Data analysis, Visualization. H. Ye: Resources provided characterization tools and analysis. R. Xiao: Supervision, Funding acquisition, Writing - review & editing.

DECLARATION OF INTERESTS

The authors declare that they have no known competing financial interests or personal relationships that could have appeared to influence the work reported in this paper.

DATA AND CODE AVAILABILITY

The data that support the findings of this study are available from the corresponding author upon reasonable request.

SUPPLEMENTAL INFORMATION

It can be found online at https://doi.org/10.59717/j.xinn-energy.2026.100178.